



OSL-thermochronometry of feldspar from the KTB borehole, Germany



Benny Guralnik^{a,b,c,*}, Mayank Jain^b, Frédéric Herman^d, Christina Ankjærgaard^c, Andrew S. Murray^e, Pierre G. Valla^d, Frank Preusser^f, Georgina E. King^d, Reuven Chen^g, Sally E. Lowick^h, Myungho Kook^b, Edward J. Rhodes^{i,j}

^a Department of Earth Sciences, ETH, 8092 Zürich, Switzerland

^b Centre for Nuclear Technologies, DTU-Risø, Frederiksborgvej 399, Building 201, 4000 Roskilde, Denmark

^c Soil Geography and Landscape group and the Netherlands Centre for Luminescence Dating, Wageningen University, Droevendaalsesteeg 3, 6708PB Wageningen, The Netherlands

^d Institute of Earth Surface Dynamics, University of Lausanne, Geopolis, 1015 Lausanne, Switzerland

^e Nordic Laboratory for Luminescence Dating, Aarhus University, Frederiksborgvej 399, Building 201, 4000 Roskilde, Denmark

^f Institute of Earth and Environmental Sciences – Geology, University of Freiburg, Albertstr. 23b, 72104 Freiburg, Germany

^g Raymond and Beverly Sackler School of Physics and Astronomy, Tel Aviv University, Tel Aviv 69978, Israel

^h Institute of Geological Sciences, University of Bern, Baltzerstrasse 1+3, 3012 Bern, Switzerland

ⁱ Department of Earth, Planetary, and Space Sciences, UCLA, Los Angeles, CA 90095-1567, USA

^j Department of Geography, University of Sheffield, Sheffield S10 2TN, UK

ARTICLE INFO

Article history:

Received 15 August 2014

Received in revised form 15 April 2015

Accepted 27 April 2015

Available online 14 May 2015

Editor: A. Yin

Keywords:

low-temperature thermochronology

OSL-thermochronology

feldspar IRSL

KTB drillhole

geothermal gradient

in-situ palaeothermometry

ABSTRACT

The reconstruction of thermal histories of rocks (thermochronometry) is a fundamental tool both in Earth science and in geological exploration. However, few methods are currently capable of resolving the low-temperature thermal evolution of the upper ~2 km of the Earth's crust. Here we introduce a new thermochronometer based on the infrared stimulated luminescence (IRSL) from feldspar, and validate the extrapolation of its response to artificial radiation and heat in the laboratory to natural environmental conditions. Specifically, we present a new detailed Na-feldspar IRSL thermochronology from a well-documented thermally-stable crustal environment at the German Continental Deep Drilling Program (KTB). There, the natural luminescence of Na-feldspar extracted from twelve borehole samples (0.1–2.3 km depth, corresponding to 10–70 °C) can be either (i) predicted within uncertainties from the current geothermal gradient, or (ii) inverted into a geothermal palaeogradient of $29 \pm 2 \text{ °C km}^{-1}$, integrating natural thermal conditions over the last ~65 ka. The demonstrated ability to invert a depth-luminescence dataset into a meaningful geothermal palaeogradient opens new venues for reconstructing recent ambient temperatures of the shallow crust (<0.3 Ma, 40–70 °C range), or for studying equally recent and rapid transient cooling in active orogens (<0.3 Ma, >200 °C Ma⁻¹ range). Although Na-feldspar IRSL is prone to field saturation in colder or slower environments, the method's primary relevance appears to be for borehole and tunnel studies, where it may offer remarkably recent (<0.3 Ma) information on the thermal structure and history of hydrothermal fields, nuclear waste repositories and hydrocarbon reservoirs.

© 2015 Elsevier B.V. All rights reserved.

1. Introduction

Many geological processes involving the cooling of rocks are recorded through the accumulation and diffusion of natural radioactivity products in certain rock-forming minerals. By quantifying such products and their associated rates of accumulation

and loss, it is possible to constrain a rock's time-temperature history, and consequently its geological evolution (Reiners and Ehlers, 2005). The recent introduction of Optically Stimulated Luminescence (OSL) dating into the family of low-temperature thermochronometers (Herman et al., 2010; Guralnik et al., 2013) has been motivated by keen interest to resolve the most recent thermal histories of bedrock on sub-Quaternary timescales, where other methods are often insensitive. Together with thermoluminescence (TL) and electron spin resonance (ESR), OSL belongs to 'trapped charge dating' (Grün, 2001), an umbrella-term for several methods concerned with quantifying the build-up of free electrical

* Corresponding author. Present address: Soil Geography and Landscape group and the Netherlands Centre for Luminescence Dating, Wageningen University, Droevendaalsesteeg 3, 6708PB Wageningen, The Netherlands.

E-mail address: benny.guralnik@gmail.com (B. Guralnik).

charge in crystalline defects and impurities, and the translation of this charge into radiometric ages. The core idea of trapped charge thermochronometry dates back to the mid-1950s, when the first correlations between TL glow-curves and the environmental or palaeoenvironmental temperatures were first noticed and described (Houtermans et al., 1957).

Initially used for meteorite classification (Grögler et al., 1958), luminescence thermochronometry was soon borrowed into diverse contexts including geological ore prospecting (e.g. Lovering, 1958), dating contact metamorphism (e.g. Johnson, 1963) and palaeoclimate reconstruction (e.g. Ronca and Zeller, 1965). The latter theme flourished during the lunar exploration era, enabling the remarkable inference of in-situ temperatures within lunar regolith (Hoyt et al., 1971; Durrani et al., 1977). Further expansion of luminescence thermochronometry into hydrothermal prospecting (e.g. Takashima, 1979), palaeoseismological inference (e.g. Ikeya et al., 1982), and hydrocarbon exploration (e.g. Ypma and Hochman, 1991), was recently superseded by studies utilising ESR or OSL signals to derive orogenic exhumation rates (Grün et al., 1999; Herman et al., 2010).

Despite its long-standing history, trapped charge thermochronometry has an apparent lack of calibration and/or validation under well-constrained laboratory and natural conditions. Thus, even the most elaborate thermal inversions were partly based on ad-hoc assumptions regarding the kinetics of electron trapping (Ronca and Zeller, 1965), the thermal stability of the electron traps (Hoyt et al., 1971), or the athermal loss pathway (Durrani et al., 1977). With the notable exception of Durrani et al. (1972, 1973), the majority of later studies circumvented the time-consuming determination of laboratory kinetics by adherence to their standard literature values and/or simplifying approximations (e.g. Grün et al., 1999; Herman et al., 2010). Thus, although several studies produced pioneering and insightful qualitative results, their projection onto absolute scales may be seen as subject for further investigation (Guralnik et al., 2013, 2015a).

In the current paper, we calibrate the response of one particular trapped charge signal (the infrared stimulated luminescence from feldspar, hereafter IRSL; Hütt et al., 1988) to radiation and heat under laboratory conditions, and verify the resulting calibration in a well-constrained ‘natural laboratory’ (the KTB borehole; Hirschmann et al., 1997). Our laboratory calibration procedure reintroduces a full signal characterisation (Durrani et al., 1972, 1973), studying in detail the response of all samples to both cumulative radiation and progressive isothermal storage. This laboratory behaviour is then fitted by a composite kinetic model (Huntley, 2006; Guralnik et al., 2015b), utilising only six physical parameters to describe >100 experimental sample-dependent observations. In contrast to previous studies which documented a decrease of TL or ESR with borehole depth (e.g. Ypma and Hochman, 1991; Prokein and Wagner, 1994; Grün et al., 1999), our data and model allow us to perform a formal inversion of IRSL into apparent storage temperatures, and compare those to independently-obtained direct measurements (e.g. Clauser et al., 1997), yielding a satisfactory match. Our paper concludes with a discussion of the sensitivity of the method, confirming the applicability of Na-feldspar IRSL to constrain recent rock palaeotemperatures in the <0.3 Ma, 40–70 °C range, which is currently rarely accessible by alternative methodologies.

2. Materials and methods

2.1. Study site and sampled depths

The KTB is a deep scientific drilling borehole in southwestern Germany, penetrating ~9 km of the Variscan crystalline basement (Hirschmann et al., 1997). The repetitive rock column at the KTB

(Fig. 1a) consists of intensely folded, foliated, and steeply dipping units of metabasite and gneiss, disclosing a long and discontinuous history of reverse faulting and supracrustal stacking (Wolfe and Stockli, 2010, and references therein). The inferred thermal stability of the site from ~25 Ma onwards (Coyle et al., 1997) offers a unique opportunity to observe various luminescence systems under the simplifying assumption of a natural dynamic equilibrium (Hoyt et al., 1971; Prokein and Wagner, 1994). In the scope of this study, the minor imprint of Pleistocene glaciations on borehole temperatures (<3 °C; Clauser et al., 1997) may be safely disregarded in light of our comparable analytical uncertainties. In a previous work, Prokein and Wagner (1994) have qualitatively described a reduction of TL in three KTB quartz samples within a depth range of 0.3–1.8 km. In the present study, we re-sampled a comparable range with an increased resolution: twelve evenly-spaced core samples were obtained from a depth range of 0.1–2.3 km (Fig. 1a and Table 1), corresponding to a thermal window of ca. 10–70 °C (Clauser et al., 1997). Our samples included seven gneisses and five amphibolites, whose representative mineralogy is shown in Figs. 1b–c.

Our target depth range (0.1–2.3 km) aimed to characterise the ‘partial retention zone’ (PRZ) of the IRSL thermochronometer, bracketing the region where apparent ages t_{app} drop from 90% to 10% of their near-surface value (e.g. Reiners and Brandon, 2006). Other thermochronological data from KTB depth of 0.1–2.3 km (Wolfe and Stockli, 2010 and references therein) is characterised by uniform apparent ages of $t_{app} \sim 370$ Ma from hornblende K–Ar and Ar/Ar ($T_C \sim 500$ °C), $t_{app} \sim 360$ Ma from muscovite K–Ar and Ar/Ar ($T_C \sim 350$ °C), $t_{app} \sim 320$ Ma from biotite K–Ar and Ar/Ar ($T_C \sim 300$ °C), $t_{app} \sim 240$ Ma from titanite fission-track ($T_C \sim 240$ °C), and $t_{app} \sim 85$ Ma from both titanite and zircon (U–Th)/He ($T_C \sim 200$ °C and ~180 °C, respectively), where T_C is the closure temperature of each thermochronometer (Dodson, 1973; Reiners and Brandon, 2006). While the two lowest-temperature systems do exhibit a significant age decrease within the 0–2.3 km depth range, with apatite fission-track ages reducing from ~70 Ma to ~50 Ma ($T_C \sim 120$ °C; Coyle et al., 1997), and apatite (U–Th)/He ages from ~55 Ma to ~22 Ma (with an abnormally high $T_C \sim 90 \pm 20$ °C; Warnock et al., 1997), this depth brackets only the top portions of their inferred partial retention zones at the KTB (Warnock et al., 1997), thus leaving the search for alternative systems with a shallower PRZ still open.

2.2. Sample preparation and luminescence instrumentation

While the intended target mineral of this study was initially quartz (cf. Prokein and Wagner, 1994; Herman et al., 2010), the observed quartz OSL was dim and further heavily overprinted by feldspar luminescence from intergrowths or inclusions (Guralnik et al., 2015a). However the feldspar IRSL measured at 50 °C (hereafter IRSL₅₀) exhibited familiar characteristics, and so we adopted the latter as a valid alternative to quartz OSL (Wallinga et al., 2000; Buylaert et al., 2011; Sohbati et al., 2013). Initially considering the increasingly popular elevated stimulation temperature protocols (e.g. Li and Li, 2011; Buylaert et al., 2012), the post-IR IRSL₂₉₀ of both the uppermost and the lowermost samples was found in field saturation, precluding further investigation of post-IR IRSL signals.

For luminescence measurements, light-unbleached feldspar crystals from the inside of each core sample were extracted by standard laboratory procedures (Supplementary Figure and Table S1), and mounted on stainless steel discs to produce large (4–6 mm) aliquots. All IRSL measurements were performed on automated Risø TL/OSL DA-15/20 readers, each possessing a ⁹⁰Sr/⁹⁰Y beta source (0.1–0.3 Gy s⁻¹) and a heater plate (20–650 °C) calibrated to within systematic uncertainties of <4% and <1%, respec-

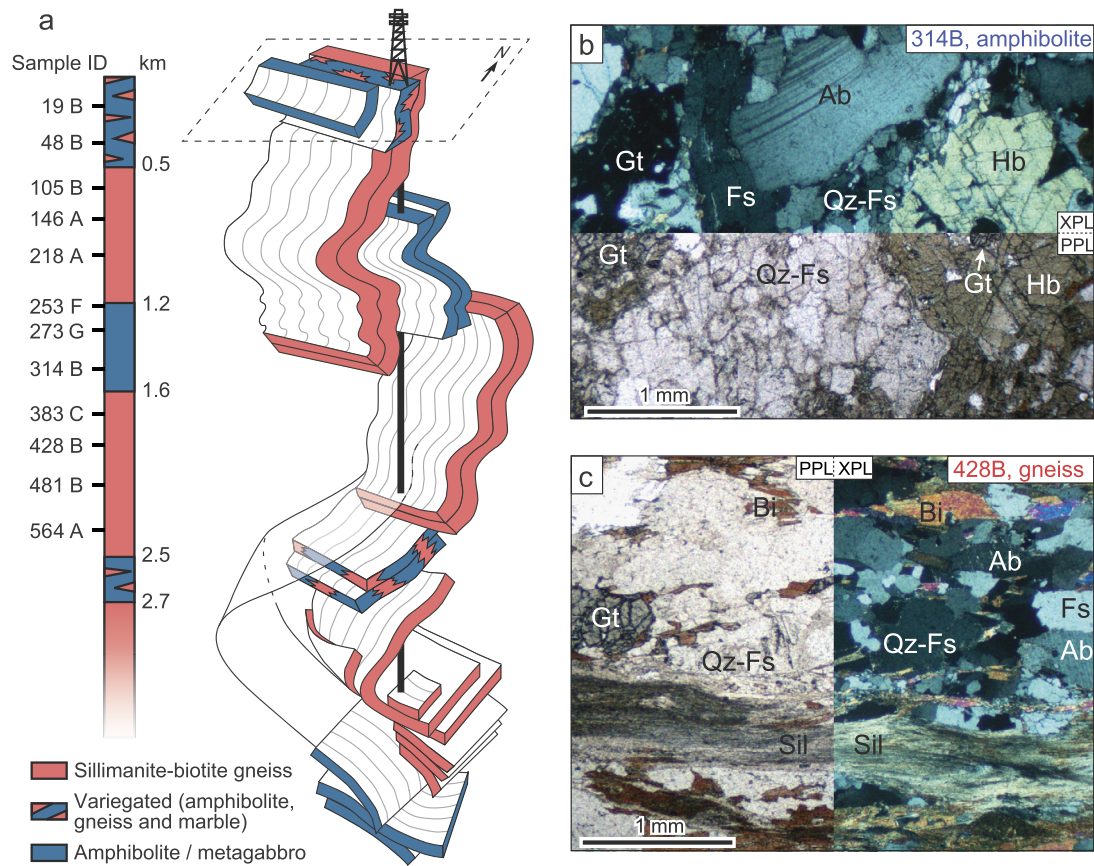


Fig. 1. (a) Schematic lithological column at the KTB (after Hirschmann et al., 1997), and sampled core depths. (b–c) Representative thin sections of an amphibolite (b) and a gneiss (c), showing a single view-field displayed half in plain (PPL), and half in cross-polarised (XPL) light. Gt – garnet, Hb – hornblende (amphibole), Qz – quartz, Fs – feldspar, Ab – albite, Bi – biotite, Sil – sillimanite.

Table 1
Overview of samples used in this study.

Sample ^a			Whole-rock radiochemistry ^b			Aliquot mineralogy ^c				Natural dose rate ^d
Depth (km)	ID	Lithology	U (ppm)	Th (ppm)	K (wt.%)	Qz (%)	Ab (%)	An (%)	Or (%)	\dot{D} (Gy ka ⁻¹)
0.146	19B	Titanite-amphibolite	0.5	1.6	0.90	38	48	3	11	1.50
0.334	48B	Clinopyroxene-amphibolite	1.3	1.7	0.38	7	68	17	9	1.03
0.566	105B	Kyanite-sillimanite-garnet-biotite-gneiss	2.2	9.3	1.49	58	25	9	9	2.92
0.726	146A	Kyanite-sillimanite-garnet-biotite-gneiss	3.2	7.3	1.24	31	44	10	15	2.84
0.911	218A	Garnet-sillimanite-biotite-gneiss	2.4	9.0	1.83	57	29	10	4	2.96
1.175	253F	Garnet-amphibolite	0.8	2.1	1.25	22	54	20	5	1.58
1.300	273G	Garnet-amphibolite	1.4	3.3	0.48	14	59	24	3	1.07
1.499	314B	Garnet-amphibolite	1.3	4.2	0.44	57	28	14	1	1.07
1.730	383C	Sillimanite-muscovite-biotite-gneiss	2.5	7.7	1.72	53	32	7	9	3.02
1.892	428B	Garnet-sillimanite-biotite-gneiss	2.6	8.9	2.42	51	38	7	4	3.44
2.097	481B	Garnet-sillimanite-biotite-gneiss	2.7	8.7	2.34	72	18	5	4	3.57
2.329	564A	Garnet-sillimanite-biotite-gneiss	2.5	7.8	2.38	45	40	11	4	3.30

^a Samples were obtained at the borehole location (49.83°N, 12.12°E, 513 masl), through GEO-Zentrum an der KTB (Am Bohrturm 2, D-92670 Windischeschenbach, Germany). Samples 19B through 383C are from core subsection VB1, and 428B through 564A from VB1a. Depth corresponds to 'true vertical depth' (± 0.5 m accuracy). Sample lithology is from on-site drilling logs, further confirmed by thin-section study under a polarising microscope.

^b Whole-rock elemental concentrations as measured on a Perkin Elmer Sciex ELAN 6100/9000 ICP-MS, with an estimated analytical precision of 3.9% (U and Th) and 1.3% (K). See Supplementary Figures and Tables S2–S3 for full geochemical report.

^c Aliquot-specific mineralogy (Qz = SiO₂, Ab = NaAlSi₃O₈, An = CaAl₂Si₂O₈, Or = KAlSi₃O₈) as measured using an XRF attachment to the Risø TL/OSL reader, with an estimated analytical precision of 7%. See Supplementary Figure and Table S4 for full XRF report.

^d Natural dose rates were calculated using the standard conversion factors of Guérin et al. (2012), and include whole-rock radioactivity due to U, Th and K, alongside the internal radioactivity of feldspar due to $K_{int} = Or/(Ab + An + Or) \times 14\%$. Water content was estimated for all samples as $2 \pm 2\%$, while contributions from alpha and cosmic radiation were considered negligible. The reported dose rates are assigned a conservative uncertainty of 15% (see text).

tively (Bøtter-Jensen et al., 2010 and references therein). Luminescence was stimulated with infrared (870 ± 40 nm) light-emitting diodes delivering ~ 135 mW cm⁻² at the sample position; lumi-

nescence was detected by a photomultiplier tube (EMI QA 9235) situated behind a combination of a 2-mm Schott BG39 and a 4-mm Corning 7-59 filters.

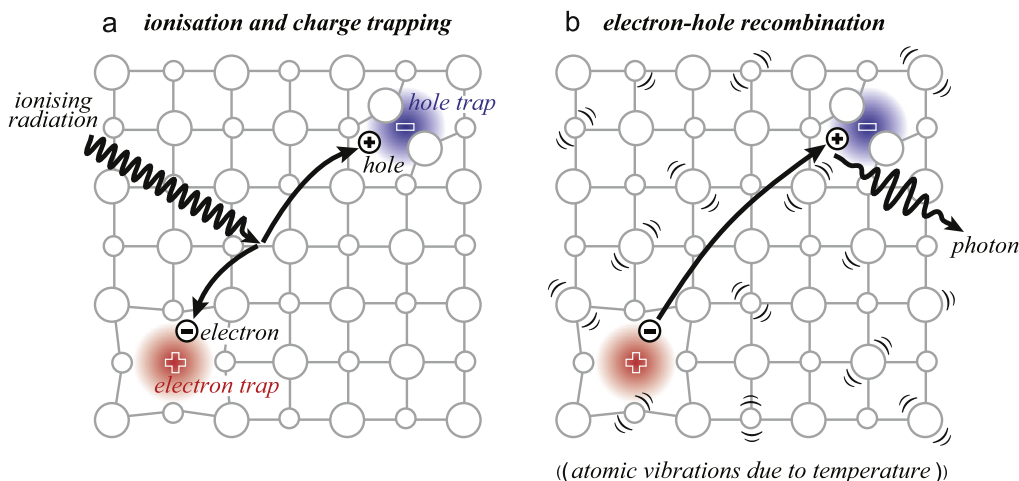


Fig. 2. Trapping and detrapping of electrons and holes in a natural crystal. (a) Interaction of ionising radiation with the crystalline lattice may displace and mobilise a valence electron, leaving a hole behind. Such free charges migrate through the crystal, until their capture in oppositely-charged lattice defects (red and blue spheres). (b) Application of heat to the crystal (shown as atomic vibrations) may remobilise a trapped electron to recombine with a hole, releasing its excess energy in form of a luminescent photon. (For interpretation of the references to colour in this figure legend, the reader is referred to the web version of this article.)

2.3. Sample chemistry and natural dose rates

Whole-rock chemistry of the twelve samples was determined using inductively-coupled plasma mass spectrometry (Supplementary Figures and Tables S2–S3), of which the dominant radionuclides are listed in Table 1 (U, Th and K). Aliquot-specific mineralogy was further assessed by an X-ray fluorescence (XRF) attachment to the Risø TL/OSL reader (Supplementary Figure and Table S4), with mineralogical breakdown to end-members also listed in Table 1 (Qz, Ab, An, and Or). Despite a considerable contamination by quartz (~40% wt. on average), further purification of feldspar was deemed unnecessary as the contribution of quartz to luminescence signals used in feldspar IRSL dating is negligible (Sohbati et al., 2013 and references therein). Since K-feldspar is extremely rare in the KTB borehole (e.g. Warnock and Zeitler, 1998), and was further uncommon in our analysed thin-sections, we interpret that the analysed feldspars (~Ab₇₀An₂₀Or₁₀ on average) were predominantly a solid-solution Na-feldspar spanning between anorthoclase and oligoclase, and not a mixture of discrete phase end-members. However, rare occurrences of K-feldspar veins and inclusions, as noted in thin-section analysis, were also taken into our dosimetric consideration as described next.

Whole-rock radionuclide concentrations U, Th, K, and the internal potassium K_{int} from within feldspar itself (as estimated from the Or/(Ab + An + Or) ratio) were converted into sample-specific environmental dose rates using standard conversion factors (Guérin et al., 2012) as follows. In general, the natural dose rates at the KTB fall on the lower end of natural radioactivity in crystalline bedrock, enabling a standard dating range of <0.3 Ma as in common sedimentary environments (e.g. Buylaert et al., 2011 and references therein). For each KTB sample, the natural dose rate \dot{D} (last column in Table 1) has been calculated as an arithmetic average over four extreme dose rate scenarios \dot{D}_1 – \dot{D}_4 (Supplementary Figure and Table S5), where \dot{D}_1 is a solid-solution Ab_xAn_yOr_z (with x , y and z from Table 1) with grain diameter $\phi = 0.1$ mm, \dot{D}_2 as above with $\phi = 2.5$ mm, \dot{D}_3 a pure K-feldspar phase (Or₁₀₀) with $\phi = 1$ μm , and \dot{D}_4 as above with $\phi = 100$ μm . Such scenario diversity arises from a combination of two factors: (i) the uncertainty in the grain size preferentially sampled by crushing a crystalline rock (compared to a more sorted grain-size in sedimentary environments), and (ii) the uncertainty regarding which feldspar phase is the actual IRSL emitter (e.g. Sohbati et al., 2013). While our thermochronometric inference remains virtually unchanged for any of the above scenarios (Supplementary Figure and Table S9), we

believe that the average-scenario dose rate \dot{D} , further assigned a generous error of 15% (corresponding to the average scatter in the Or/(Ab + An + Or) ratio as determined by XRF), is a guiding representative value which firmly encompasses all of the envisaged dosimetric possibilities.

3. Luminescence response to radiation and heat

3.1. The principle of luminescence dating

Luminescence dating utilises the natural capacity of some lattice defects and impurities to cumulatively store free electrical charge as continuously produced by environmental radiation. Application of heat or light to a crystal with trapped charge results in the emission of TL or OSL, respectively. An atomic-scale description of luminescence may be illustrated by considering two simple defects in an alkali halide lattice (blue and red spheres in Fig. 2), corresponding to two oppositely charged ‘traps’. A quantum of ionising energy (incident black wave in Fig. 2a) may displace an electron from its valence bond, setting the electron and its counterpart ‘hole’ in motion until they are decelerated by the electromagnetic fields of oppositely-charged defects encountered on their way. While trapped holes remain generally immobile (Chen and Pagonis, 2011), trapped electrons can often be remobilised again, either by application of external energy such as heat (depicted in Fig. 2b), light, or through a purely spontaneous process of quantum-mechanical tunnelling (Huntley, 2006), the latter typically occurring in low-order crystallographies including feldspar. Fig. 2b illustrates the detrapping of an electron due to lattice vibrations at an elevated temperature, which remobilises the electron and sets it in motion until it either re-traps or recombines with a trapped hole, while in the latter case emitting a luminescent photon (black wavelet in Fig. 2b). Assuming negligible re-trapping of electrons once optically evicted from their traps, the luminescence light sum L may be regarded as a proxy for the number of trapped electrons n , i.e. $L \propto n$ (Chen and Pagonis, 2011), and hence for the duration of the mineral’s exposure to ionising radiation since the trap was last emptied (Aitken, 1998).

3.2. Characterisation of luminescence behaviour in the laboratory

The slow accumulation and emptying of electron traps in a mineral in nature can be studied under laboratory-accelerated conditions using artificial sources of radioactivity and heat, relying

Table 2Luminescence protocols for measurement of the feldspar IRSL₅₀ kinetics in the laboratory.

Radiation response (SAR method ^a)	Isothermal response (Short-shine method ^b)
1. Give dose D_x	1. IRSL at 290 °C for 200 s
2. Preheat (5°C s^{-1}) to 250 °C, hold for 60 s	2. Give test dose D_{test}
3. IRSL at 50 °C for 200 s $\rightarrow L_x$	3. Preheat (5°C s^{-1}) to 250 °C, hold for 60 s
4. Give test dose D_{test}	4. Hold at $T^\circ\text{C}$ for t_x s
5. Preheat (5°C s^{-1}) to 250 °C, hold for 60 s	5. IRSL at 50 °C for 0.1 s $\rightarrow L_x$
6. IRSL at 50 °C for 200 s $\rightarrow T_x$	6. Return to step 4
7. IRSL at 290 °C for 200 s	7. IRSL at 290 °C for 200 s
8. Return to step 1	8. Give test dose D_{test}
	9. Preheat (5°C s^{-1}) to 250 °C, hold for 60 s
	10. IRSL at 50 °C for 0.1 s $\rightarrow T_x$
	11. Return to step 10

^a Adapted from Wallinga et al. (2000). The target irradiation doses were $D = [0, 0.02, 0.04, 0.08, 0.16, 0.32, 0.64, 1.28, 2.56, 0, 0.04]$ kGy, and the test dose was $D_{\text{test}} = 0.04$ kGy; corresponding irradiation times were calculated via $t_x = D_x/\dot{D}$, where \dot{D} is the laboratory dose rate (instrument-specific). For samples near saturation, ~ 5 and ~ 10 kGy doses were further administered to better characterise $L_{\text{nat}}/L_{\text{labmax}}$. The first and the penultimate zero-doses (no irradiation) extract the natural dose (stars in Fig. 3a) and signal recuperation, respectively. L_x and T_x were derived by integrating the first 100 s (signal) and the following 100 s (background) of the stimulation curve.

^b Adapted from Auclair et al. (2003). For high-temperature experiments ($T = 170, 190$ and 210°C), the test dose was $D_{\text{test}} = 0.03$ kGy, and the holding times were $t_x = 10 \times 2^{x-1}$, where $x = [-\infty, 0, 1, 2, \dots, 10]$. For the room-temperature experiments ($T \approx 15^\circ\text{C}$), $D_{\text{test}} = 0.09$ kGy, and $t_x \approx 10^{2.34+0.37x}$, where $x = [1, 2, \dots, 8]$. L_x and T_x were derived by integrating the entire stimulation period of 0.1 s minus a background of 20 ms immediately following LED turn-off.

Note: The normalised luminescence L in the vertical axis of Figs. 3a and 3b corresponds to arbitrarily scaled L_x/T_x data (for presentational purposes).

on the fundamental geochronometric assumption that the system behaviour is governed by the same physical laws across many orders of magnitude of kinetic rates (e.g. Reiners and Ehlers, 2005; Chen and Pagonis, 2011). To determine the growth of feldspar IRSL₅₀ as a function of cumulative irradiation, we used a common modification of the Wallinga et al.'s (2000) Single Aliquot Regenerative-dose (SAR) protocol for feldspar IRSL₅₀ (Table 2, left column). In the scope of this study, the minor systematic effect of irradiation temperature on the ionisation cross section of feldspar IRSL₅₀ (<10% effect in the 0–80 °C range; Wallinga et al., 2002) was not considered significant due to the logarithmic relationship between dose rate and apparent palaeotemperature (Hoyt et al., 1971; Guralnik et al., 2013). Thus, all samples were irradiated at room temperature as in standard feldspar IRSL dating, leaving the assessment of minor effects due to elevated-temperature irradiation for more technical studies in the future. To determine the decrease of luminescence as a function of cumulative isothermal storage, we replaced the SAR fading protocol of Murray et al. (2009) with the short-shine isothermal decay experiment of Auclair et al. (2003), favouring the latter time-saving procedure (Table 2, right column) in light of indistinguishable data obtained by both methods during preliminary testing. Aiming to constrain the mirroring effects of electron trapping and detrapping across the widest experimentally-feasible time domain, both protocols in Table 2 were adjusted to sample the luminescence response evenly across 3–4 orders of magnitude of time. Standard quality criteria included rejection of a few self-inconsistent measurements, in which dose recycling and/or dose recovery deviated from unity by more than 10% (e.g. Buylaert et al., 2011, and references therein).

Representative Na-feldspar IRSL₅₀ response to radiation and isothermal storage is shown for sample 481B in Fig. 3a–b. The assessment of the radiation-response (Fig. 3a) begins with the measurement of the sample's natural luminescence L_{nat} (stars in Fig. 3a), after which a series of laboratory-regenerated luminescence intensities L is measured for increasing ionising doses (circles in Fig. 3a). Figure 3a contains SAR data for three different aliquots of the same sample, each measured on a different luminescence reader (hence the different laboratory dose rates quoted in the figure). The demonstrated accuracy of $\sim 5\%$ of the SAR protocol in recovering known dose from all samples (Supplementary Figure and Table S7) increased our confidence, that the natural

luminescence light-sums (stars in Fig. 3a) may be trusted to obtain radiometric ages and/or palaeotemperatures. The mirroring process of isothermal response (Fig. 3b) was measured only on one aliquot per sample (due to excellent reproducibility across aliquots), monitoring the decay of laboratory-regenerated luminescence as a function of cumulative storage times at 15 °C, 190 °C, 210 °C and 230 °C, respectively.

3.3. Kinetic model of luminescence response

To quantitatively describe luminescence response in the laboratory (Figs. 3a–b, and Supplementary Figures and Tables S6–1 through S6–12), we consider the trapping of n electrons in N available traps (Hoyt et al., 1971); the traps have the characteristic dose D_0 [Gy], the Arrhenius parameters E [eV] and s [s^{-1}], and are binned by their separation distance r' [dimensionless] to their nearest-neighbouring hole (Huntley, 2006). Denoting $\hat{n}(r') = n(r')/N(r')$ as the fraction of occupied traps at a given electron-hole separation distance, we can express the concurrent electron trapping and detrapping via:

$$\frac{\partial \hat{n}(r')}{\partial t} = \frac{\dot{D}}{D_0} [1 - \hat{n}(r')]^\alpha - se^{-E/k_B T} [\hat{n}(r')]^\beta - se^{-\rho'^{-1/3} r'} [\hat{n}(r')] \quad (1)$$

where t [s] and T [K] are time and temperature, \dot{D} [Gys^{-1}] the ionising dose rate, ρ' [dimensionless] the scaled density of the hole centres, α and β [dimensionless, ≥ 1] the kinetic orders of trapping and detrapping (Guralnik et al., 2015b), and k_B [eVK^{-1}] is Boltzmann's constant. The first right hand side (RHS) term in Eq. (1) links the trap filling rate to the fraction of unoccupied traps, $1 - \hat{n}(r')$; the second and third RHS terms link the rates of the thermal and athermal trap emptying to the relative trap occupancy itself, $\hat{n}(r')$. All model constants governing electron trapping and detrapping are further listed and explained in Table 3, alongside their representative averages across all KTB samples studied here.

To obtain the instantaneous total trap filling $\hat{n}(t)$ in the entire crystal, the solution of Eq. (1) is typically summed over ~ 100 equally-spaced separation distances $0 < r' < 2$ (cf. Kars et al., 2008):

$$\hat{n}(t) = \sum_{r'} \hat{n}(r', t) \times 3(r')^2 \exp[-(r')^3] \quad (2)$$

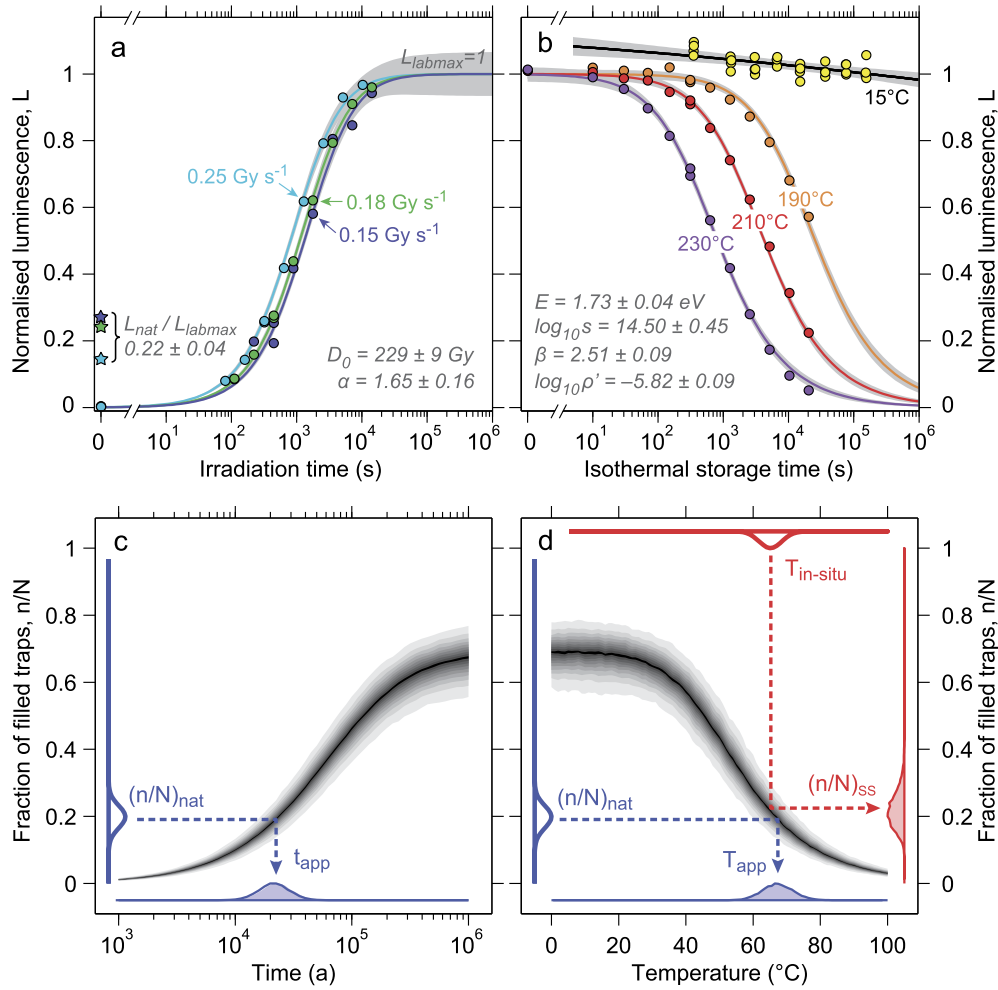


Fig. 3. Representative laboratory luminescence measurements collected by protocols listed in Table 2, here illustrated for sample 481B: (a) The normalised IRSL₅₀ response of the crystal due to increasing exposure to ionising irradiation shown for three different laboratory dose rates (circles represent regenerated dose points, stars correspond to the natural signal). (b) The normalised decay of IRSL₅₀ of a single aliquot following its exposure to isothermal heat at 15, 190, 210, and 230 °C. All the >100 experimental data points (solid circles in a and b) can be fitted with Eqs. (1)–(2) (thin lines and shaded 95% confidence interval contours) using only six model parameters (listed in Tables 3–4). (c) Projection of the measured natural trap filling $(n/N)_{\text{nat}}$ (vertical distribution in hollow blue) onto the joint distribution of modelled age-concentration pairs $(t, n/N)$ (greyscale probability field, corresponding to $\sim 10^6$ Monte Carlo randomised instances) produces the apparent age t_{app} (horizontal distribution in filled blue). (d) Observed values $T_{\text{in-situ}}$ and $(n/N)_{\text{nat}}$ (top and left hollow distributions, respectively) are projected onto the modelled temperature-concentration pairs $(T, n/N)$ (greyscale probability field) to obtain model prediction for the trap filling at thermal steady-state $(n/N)_{\text{ss}}$ (red filled distribution on the right), and the model inversion of the apparent storage temperature T_{app} (blue filled distribution at the bottom). (For interpretation of the references to colour in this figure legend, the reader is referred to the web version of this article.)

Table 3

Kinetic model parameters of the Na-feldspar IRSL₅₀ thermochronometer.

Parameter	Description	KTB average $\pm 1\sigma$	Units
\dot{D}	Ionising dose rate	$2.4 \pm 1.0 \text{ Gy ka}^{-1}$	Gy ka^{-1} (nature) or Gy s^{-1} (laboratory)
D_0	Characteristic ('saturation') dose	213 ± 54	Gy
α	Kinetic order of electron trapping	1.7 ± 0.2	-
E	Thermal activation energy	1.7 ± 0.1	eV
s	Attempt-to-escape frequency	$10^{14.5 \pm 0.6}$	s^{-1}
β	Kinetic order of thermal electron detrapping	2.6 ± 0.3	-
ρ'	Scaled hole density	$10^{-6.0 \pm 0.9}$	-

Reported values summarise the KTB best-fit parameters (columns 4–9 of Table 4).

in which $3(r')^2 \exp[-(r')^3]$ is the probability of r' to occur in the crystal (Huntley, 2006). Eqs. (1)–(2) represent a straightforward combination of (i) the general-order reformulation (Guralnik et al., 2015b) of the classical first-order luminescence kinetics (Hoyt et al., 1971), and (ii) the athermal loss model of Huntley (2006). Note that under simplifying assumptions, Eqs. (1)–(2) reduce to familiar cases: the first-order kinetic model shared by all trapped charge methods (Guralnik et al., 2013) may be obtained by solving

Eq. (1) with $\alpha = \beta = 1, \rho' \rightarrow 0$; conversely, solving Eqs. (1)–(2) with $\alpha = 1, E \rightarrow \infty$ replicates the fading model of Kars et al. (2008). While a similar treatment to Eqs. (1)–(2) has previously only been found in Durrani et al. (1977), we believe that the adopted rate equations are a generalised formulation of a long-accepted theory.

Sample-specific kinetic parameters were obtained by non-linear least square fitting of the laboratory-regenerated IRSL₅₀ signals

Table 4
Natural luminescence levels, best-fit kinetic parameters, and apparent ages of feldspar IRSL₅₀.

Measurements									Model				
Sample		Natural luminescence ^a	Best-fit kinetic parameters ^b describing laboratory behaviour						Natural trap filling	Inverted age and temperature ^c		Predicted trap filling in nature ^d	
Depth (km)	ID	L_{nat}/L_{labmax}	D_0 (Gy)	α	E (eV)	$\log_{10} s$ (s in s^{-1})	β	$\log_{10} \rho'$	$(n/N)_{nat}$	t_{min} or t_{app} (ka)	T_{max} or T_{app} (°C)	$T_{in-situ}$ (°C)	$(n/N)_{ss}$
0.146	19B	0.80 ± 0.04	171	1.81	1.75	14.28	3.28	−5.89	0.74 ± 0.03	>403 ⁺⁴⁵⁶ _{−100}	<41 ⁺⁴ _{−7}	12 ± 1	0.74 ^{+0.03} _{−0.05}
0.334	48B	1.00 ± 0.05	82	1.27	1.79	14.80	3.06	−8.58	1.00 ± 0.05	>169 ⁺¹⁸¹ _{−47}	<51 ⁺⁴ _{−10}	17 ± 1	1.00 ^{+0.00} _{−0.01}
0.566	105B	0.87 ± 0.04	179	1.52	1.83	15.65	2.37	−6.17	0.83 ± 0.04	>133 ⁺²⁶² _{−45}	<47 ⁺⁷ _{−14}	23 ± 2	0.93 ^{+0.02} _{−0.12}
0.726	146A	0.54 ± 0.03	259	2.10	1.71	14.28	2.72	−5.55	0.44 ± 0.02	>415 ⁺⁴⁸⁵ _{−115}	<34 ⁺⁴ _{−5}	28 ± 2	0.46 ^{+0.03} _{−0.03}
0.911	218A	0.63 ± 0.03	241	1.63	1.74	14.60	2.54	−5.68	0.54 ± 0.02	>260 ⁺¹⁶⁶ _{−59}	<39 ⁺³ _{−5}	33 ± 2	0.55 ^{+0.03} _{−0.03}
1.175	253F	0.42 ± 0.03	235	1.63	1.72	14.45	2.44	−5.57	0.35 ± 0.02	205 ⁺¹¹² _{−34}	42 ⁺³ _{−5}	40 ± 2	0.36 ^{+0.05} _{−0.04}
1.300	273G	0.38 ± 0.04	201	1.71	1.72	14.52	2.42	−5.54	0.31 ± 0.03	247 ⁺¹¹⁷ _{−46}	42 ⁺³ _{−5}	43 ± 2	0.29 ^{+0.04} _{−0.04}
1.499	314B	0.19 ± 0.03	298	1.86	1.58	12.99	2.90	−5.30	0.14 ± 0.02	160 ⁺⁶³ _{−33}	45 ⁺⁵ _{−6}	49 ± 3	0.10 ^{+0.03} _{−0.02}
1.730	383C	0.36 ± 0.06	200	1.69	1.73	14.56	2.35	−5.87	0.33 ± 0.05	49 ⁺¹⁴ _{−10}	56 ⁺³ _{−3}	55 ± 3	0.33 ^{+0.05} _{−0.04}
1.892	428B	0.34 ± 0.02	225	1.63	1.74	14.62	2.39	−5.86	0.31 ± 0.02	42 ⁺⁸ _{−6}	59 ⁺² _{−2}	60 ± 3	0.28 ^{+0.05} _{−0.04}
2.097	481B	0.22 ± 0.04	229	1.65	1.73	14.50	2.51	−5.82	0.20 ± 0.03	23 ⁺⁵ _{−4}	67 ⁺³ _{−3}	65 ± 3	0.20 ^{+0.04} _{−0.03}
2.329	564A	0.13 ± 0.01	236	1.97	1.74	14.58	2.49	−5.76	0.12 ± 0.01	14 ⁺² _{−2}	74 ⁺² _{−2}	72 ± 4	0.13 ^{+0.03} _{−0.02}

^a L_{labmax} is an arbitrary aliquot-specific value, obtained through fitting and used for normalisation.

^b Best-fit kinetic parameters as obtained through simultaneous fitting of Eqs. (1)–(2) to sample-specific experimental data (collected using the protocols listed in Table 2). The R^2 of all fits lies in the range of 0.97–0.99, yielding typical parameter uncertainties of <3%.

^c Conversion of natural luminescence $(n/N)_{nat}$ into apparent age t_{app} and storage temperature T_{app} was done through Monte Carlo simulations of Eqs. (1)–(2), as further illustrated by the blue arrows in Fig. 3c and 3d, respectively. For samples in field saturation, limiting ages t_{min} and corresponding limiting temperatures T_{max} were calculated for 85% of field-saturation and are listed with > or < signs.

^d Conversion of present-day borehole temperatures $T_{in-situ}$ into predicted luminescence in thermal steady-state $(n/N)_{ss}$ was done through Monte Carlo simulations of Eqs. (1)–(2), as further illustrated by the red arrow in Fig. 3d.

(circles in Figs. 3a–b; excluding stars) using three special cases of Eqs. (1)–(2). In particular, we assumed:

- negligible electron detrapping ($\rho' \rightarrow 0$, $E \rightarrow \infty$) during laboratory irradiation,
- negligible trapping and athermal detrapping ($\dot{D} = 0$, $\rho' \rightarrow 0$) during high-temperature isothermal holding, and
- negligible trapping and thermal detrapping ($\dot{D} = 0$, $E \rightarrow \infty$) during the room-temperature isothermal holding (fading).

The above standard assumptions enable us to simultaneously fit all the SAR data using Eq. (10) in Guralnik et al. (2015b), all the high-temperature isothermal holding experiments using Eq. (11) in Guralnik et al. (2015b), and all the room-temperature fading using Eq. (7) in Huntley (2006), with s taken from the high-temperature best-fit.

The best-fit parameters for sample 481B are quoted in Fig. 3a and 3b. The obtained characteristic dose of $D_0 = 229 \pm 9$ Gy, and the Arrhenius parameters $E = 1.73 \pm 0.04$ eV and $s = 10^{14.50 \pm 0.47} s^{-1}$ fall within their familiar ranges for feldspar IRSL₅₀ (e.g. Murray et al., 2009; Sohbaty et al., 2013; Guralnik et al., 2015b, and references therein). Both kinetic orders $\alpha = 1.65 \pm 0.16$ and $\beta = 2.51 \pm 0.09$ fall within familiar ranges, indicating an appreciable departure from first-order behaviour when the electron traps are nearly empty or nearly full (Guralnik et al., 2015b). Finally, the electron-hole density of $\rho' = 10^{-5.82 \pm 0.09}$ is comparable to that reported by Kars et al. (2008) and studies citing it. The combined coefficient of determination for the entire fit ($R^2 = 0.99$) increases our confidence in further extrapolating these experimental kinetic parameters to natural conditions (where electron trapping and detrapping occur ~ 10 orders of magnitude slower than in the laboratory). The natural luminescence and best-fit kinetic parameters for all twelve depth samples are listed in Table 4, suggesting a rather universal kinetic behaviour of Na-feldspar IRSL₅₀

signals regardless of their depth, parent lithology, or feldspar mineralogy (see also Supplementary Figure and Table S10).

3.4. Estimation of the natural trap filling and its translation into apparent age and temperature

To convert the normalised natural luminescence L_{nat} into the natural trap occupancy $(n/N)_{nat}$, we use the proportionality between luminescence and trapped charge $L \propto n$ to write:

$$\frac{L_{nat}}{L_{labmax}} = \frac{(n/N)_{nat}}{(n/N)_{labmax}} \quad (3)$$

The left-hand side in Eq. (3) (stars in Fig. 3a) is obtained by dividing the measured L_{nat} by L_{labmax} as estimated from the best-fit to laboratory data. To obtain $(n/N)_{labmax}$, one simply evaluates Eqs. (1)–(2) at $t \rightarrow \infty$ after substituting the corresponding kinetic parameters and the corresponding laboratory dose rate. For sample 481B, we obtain $(n/N)_{labmax} \cong 0.86$, which attests to the fact that even after prolonged and intensive laboratory irradiation, $\sim 14\%$ of the electron traps in the crystal remain vacant due to athermal fading effects. The above $(n/N)_{labmax} \cong 0.86$ is multiplied by the observed $L_{nat}/L_{labmax} = 0.22 \pm 0.04$ to obtain the desired $(n/N)_{nat} = 0.20 \pm 0.03$. Across all samples (Table 4), the $(n/N)_{nat}$ values are $\sim 12\%$ systematically lower than their corresponding L_{nat}/L_{labmax} . Such $(n/N)_{nat}$ are fully analogous to the daughter/parent ratio in other radiogenic systems, and may be further interpreted as apparent age t_{app} or apparent storage temperature T_{app} (Guralnik et al., 2013).

In a first-order system ($\alpha = \beta = 1$) with no athermal losses ($\rho' \rightarrow 0$), the conversion of $(n/N)_{nat}$ into t_{app} or T_{app} is given by simple analytical formulae (Christodoulides et al., 1971; Guralnik et al., 2013). For the general case of Eqs. (1)–(2), however, a numerical solution is unavoidable. Note that since the reported $(n/N)_{nat}$ are corrected for the athermal electron loss pathway (via

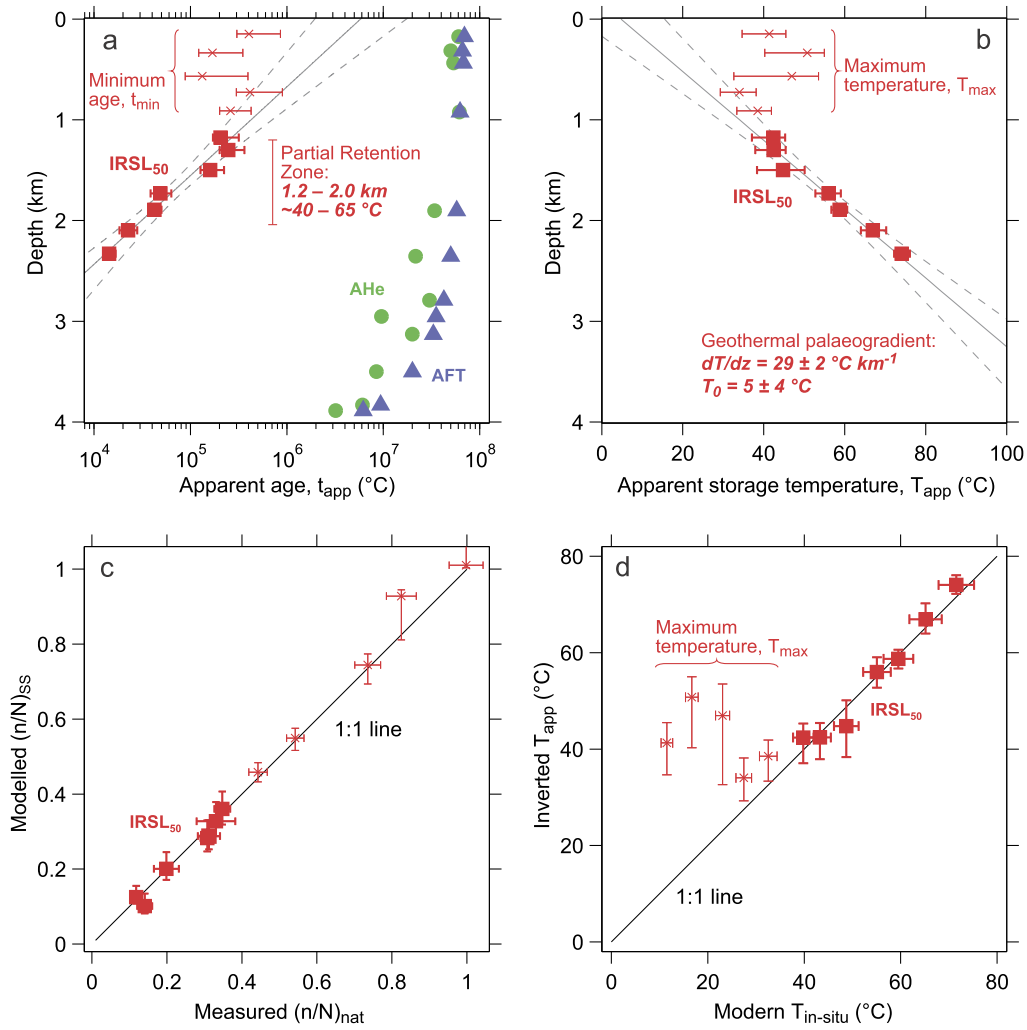


Fig. 4. (a) Downhole apparent ages of Na-feldspar IRSL₅₀ (solid squares and thin crosses; this work), apatite (U–Th)/He (circles; Warnock et al., 1997) and apatite fission track (triangles; Warnock et al., 1997). The IRSL data indiscernible from steady-state are represented by minimum ages (thin crosses), corresponding to an age equivalent of 85% of the steady-state IRSL signal (Guralnik et al., 2015a). The top 1 km of the borehole (<35 °C) is characterised by a minimum IRSL age of 0.28 ± 0.06 Ma. Note that the IRSL ages (14–430 ka) are not only younger by 2–4 orders of magnitude compared to the apatite thermochronometers, but here at KTB also display a shallower Partial Retention Zone (PRZ ~1.2–2.0 km, or 40–65 °C, as estimated from linear regression). (b) Apparent storage temperatures T_{app} as a function of depth, with a further regressed geothermal palaeogradient only through the finite temperature inversions (solid squares), amounting to $dT/dz = 29 \pm 2$ °C km⁻¹ and a surface palaeotemperature of $T_0 = 5 \pm 4$ °C. (c) laboratory-determined $(n/N)_{nat}$ (x-axis) plotted against predicted trap-filling levels at thermal steady state $(n/N)_{SS}$ (y-axis), based on a geothermal gradient of $dT/dz = 27.5 \pm 1.5$ °C km⁻¹ and $T_0 = 7.5 \pm 1.2$ °C; within uncertainties all model predictions (including near-saturated signals marked as thin crosses) fall within their corresponding laboratory determinations. (d) Modern estimates of borehole temperature (x-axis) plotted against apparent storage temperatures T_{app} (y-axis), as inverted from luminescence data. Above ~40 °C, modelled palaeotemperatures coincide with present-day measurements; below ~40 °C, only maximum temperatures (thin crosses) may be reported; the departure of T_{max} from the 1:1 line does not imply an inconsistent result but on the contrary: all present-day temperatures are safely below their maximum estimates from the IRSL₅₀ data.

Eq. (3)), our obtained t_{app} are conceptually identical to the fading-corrected ages derived from the Kars et al. (2008) model; correspondingly, our inverted storage temperatures T_{app} are similarly ‘fading-corrected’ (cf. Durrani et al., 1977).

To propagate all the uncertainties in \dot{D} , D_0 , α , E , s , β , and ρ' of a particular sample into the numerical solution of its t_{app} and T_{app} , we used Monte Carlo simulations with randomised input. Generating $\sim 10^6$ randomised realisations of the natural dose rate \dot{D} , and the best-fit kinetic parameters D_0 , α , E , s , β , and ρ' for a particular sample (fitting covariances preserved after Iman and Conover, 1982), we subjected each randomised input to (i) an athermal ($E \rightarrow \infty$) instance of Eqs. (1)–(2) for a random time of $1 \text{ ka} \leq t \leq 10 \text{ Ma}$, and (ii) a thermal steady state ($t \rightarrow \infty$) instance of Eqs. (1)–(2) for a random temperature of $0^\circ\text{C} \leq T \leq 120^\circ\text{C}$. The $\sim 10^6$ simulations of $(t, n/N)$ and $(T, n/N)$ for sample 481B are visualised as two probability density fields in Figs. 3c and 3d, respectively, the darkest shades corresponding to the highest

occurrence of simulated values. To obtain the apparent age, we project the natural trap filling $(n/N)_{nat}$ onto the joint distribution of simulated $(t, n/N)$ values to obtain an estimate of t_{app} (blue arrow in Fig. 3c). The apparent storage temperature is similarly derived by projecting $(n/N)_{nat}$ onto $(T, n/N)$ to obtain an estimate of T_{app} (blue arrow in Fig. 3d). Finally, by projecting a known storage temperature $T_{in-situ}$ onto $(T, n/N)$, the expected trap filling level at a thermal field steady-state $(n/N)_{SS}$ is obtained (red arrow in Fig. 3d). All estimated distributions (t_{app} , T_{app} , and $(n/N)_{SS}$) were fitted with asymmetrical Gaussian peaks and are reported accordingly in Table 4.

The top five samples appear to be in field-saturation (see Supplementary Figure and Table S8), and for those we obtained conservative minimum ages t_{min} (the so-called ‘2D₀ ages’; thin crosses in Fig. 4a) and maximum storage temperatures T_{max} (thin crosses in Fig. 4b) by projecting $0.85 \times n(t \rightarrow \infty)/N$ values instead of $(n/N)_{nat}$ onto the respective probability density fields (Guralnik et

al., 2015a and references therein). Note that although such minimum ages and maximum temperatures (thin crosses in Fig. 4, and “>” or “<” values in Table 4) do yield useful limiting values, these boundary estimates cannot be directly compared to the rest of the finite age/temperature dataset, thus justifying the different notation and the different graphical symbols for the two groups.

4. Validation of the feldspar IRSL₅₀-thermochronometer at the KTB

The apparent t_{app} and minimum t_{min} ages (solid squares and thin crosses in Fig. 4a), and the apparent T_{app} and maximum T_{max} storage temperatures (solid squares and thin crosses in Fig. 4b) for the twelve borehole samples may be evaluated against other available data to derive key observations as follows:

- (i) Na-feldspar IRSL₅₀ apparent t_{app} and minimum t_{min} ages are 2–4 orders of magnitude younger than the finite ages from the apatite (U–Th)/He and fission track systems (red, green and blue symbols in Fig. 4a).
- (ii) The shallowest five samples (the top ~1 km) appear in field saturation (Huntley and Lian, 2006; also see Supplementary Figure and Table S8), giving rise to only t_{min} and T_{max} estimates. These set useful limiting values but cannot be directly compared to the other finite ages/temperatures. The limiting age and temperature are $t_{min} = 0.28 \pm 0.06$ Ma and $T_{max} = 42 \pm 3$ °C (top 1 km average), comparing well with the conservative dating limit of feldspar IRSL (e.g. ~0.3 Ma in Buylaert et al., 2011), and with the thermal sensitivity threshold of quartz OSL thermochronometry (e.g. ~50 °C for the fast component; see Fig. 3b in Guralnik et al., 2015a).
- (iii) The seven deepest samples (>1.1 km depth) are characterised by apparent ages dropping from $t_{app} \sim 200$ ka at 1.1–1.5 km to $t_{app} \sim 10$ ka at 2.3 km, and by a mirroring trend in the apparent temperatures increasing from $T_{app} \sim 40$ °C at 1.1–1.5 km to $T_{app} \sim 75$ °C at 2.3 km. Linear regressions through these data place the partial retention zone (PRZ) of Na-feldspar IRSL₅₀ at ~40–65 °C (Fig. 4a), and recover a geothermal palaeogradient of $dT/dz = 29 \pm 2$ °Ckm⁻¹ with an apparent surface temperature of $T_0 = 5 \pm 4$ °C (Fig. 4b). This inverted palaeogradient agrees well with direct long-term temperature monitoring ($dT/dz = 27.5 \pm 1.5$ °C and $T_0 = 7.5 \pm 1.2$ °C in Clauser et al., 1997) as well as with other thermochronometric data (e.g. Coyle et al., 1997), but raises the question over what timescale the inverted palaeogradient is valid. To make a conservative estimate across samples with different equilibration times (roughly proportional to t_{app}), we report the log-average of their corresponding IRSL₅₀ ages as the minimal period (the last ~65 ka), over which the inverted palaeogradient is believed to be representative.

The extrapolation of laboratory kinetics to natural conditions is further examined and verified in Figs. 4c–d. Figure 4c shows that if we assume that the present-day geothermal gradient remained unchanged in the last ~1 Ma, the observed natural trap filling levels $(n/N)_{nat}$ in all twelve depths are within analytical error of their model predictions at thermal steady state $(n/N)_{SS}$. Conversely, but still assuming thermal steady-state conditions at the borehole, all the successfully inverted apparent temperatures T_{app} are shown to overlap with their present day temperature, $T_{in-situ}$ (Fig. 4d). The top five samples categorised as in field saturation (Supplementary Fig. and Table S8), correctly yield T_{max} which within uncertainties are all higher than the modern in-situ temperatures, rendering these conservative estimates as correct.

5. Applicability in diverse geological environments

Following the demonstrated validity of extrapolating the laboratory kinetics of Na-feldspar IRSL₅₀ to natural conditions, we proceed to explore the temperatures, timescales and rates on which Na-feldspar IRSL₅₀ can resolve ambient or transient thermal histories. For all subsequent simulations, we consider a representative Na-feldspar IRSL₅₀ behaviour by using the KTB-average kinetic parameters as reported in Table 3.

We begin by approximating thermal equilibrium conditions by simulating a 1 Ma isothermal storage in a synthetic borehole, and compare Na-feldspar IRSL₅₀ ages to equivalent predictions for apatite (U–Th)/He and fission-track systems (Fig. 5a). The thin segment of IRSL₅₀ ages is conservatively considered beyond the reliable dating limit (due to field saturation; Huntley and Lian, 2006). The transition between a dateable and field-saturated Na-feldspar IRSL₅₀ system (right annotated corner in Fig. 5a) corresponds to a storage temperature of 32 °C and an apparent age of 0.33 Ma. This implies that theoretically, feldspar IRSL₅₀ apparent ages and storage temperatures may be extracted from conditions where ambient temperature exceeds 32 °C, i.e. typically >1 km depth, which is in broad agreement with the experimental results in Fig. 4a–b.

The response of the Na-feldspar IRSL₅₀ thermochronometer to monotonic cooling is studied next through the ‘closure temperature’ concept (Dodson, 1973; Guralnik et al., 2013). Closure temperatures T_C of the Na-feldspar IRSL₅₀ system (numerically evaluated using Eq. (5) in Guralnik et al., 2013 for $T_P = 0$ °C) are shown in Fig. 5b alongside the conservative estimates of T_C in apatite (U–Th)/He and fission-track systems (calculated using representative Arrhenius parameters; see caption to Fig. 5). The threshold between a dateable and field-saturated Na-feldspar IRSL₅₀ system (right annotated corner in Fig. 5b) is a cooling rate of 190 °C Ma⁻¹, corresponding to a closure temperature of $T_{C,190} = 53$ °C. Na-feldspar IRSL₅₀ systems cooling faster would be dateable when emerged at a surface of $T_P = 0$ °C; those cooling slower will provide only limiting values ($t_{min} \sim 0.33$ Ma or $T_{max} \sim 32$ °C). Note that since the cooling rate threshold is a function of the final cooling temperature, T_P (Guralnik et al., 2013), an elevated T_P of 40 °C would theoretically shift the detectability threshold down to ~100 °C Ma⁻¹. Note, that although for the baseline cooling rate of 10 °C Ma⁻¹, the closure temperature of Na-feldspar IRSL₅₀ is $T_{C,10} = 23$ °C (left annotated corner in Fig. 5b), this metric is potentially misleading (Guralnik et al., 2013) since a feldspar IRSL₅₀ system cooling at this rate is expected to be in field-saturation by the time that it reaches the surface of Earth.

Several examples of representative thermal histories and the associated build-up of Na-feldspar IRSL₅₀ trap occupancy are studied in Fig. 5c and 5d, respectively (note matching indexing i–vi in both figures for clarity). Three scenarios (i–iii) result in a final trap occupancy of $n/N = 0.75$ and a minimum age of $t_{min} = 0.27$ Ma. Conversely, scenarios (iv–vi) result in a final trap occupancy of $n/N = 0.50$ with possible interpretations of $t_{app} = 125$ ka and $T_{app} = 42$ °C; however, further discrimination between these scenarios (iv–vi) is impossible without independent constraints. The notion that feldspar IRSL₅₀ systems are overprinted by the last thermal event occurring in the most recent ~0.3 Ma may be appreciated from a side-by-side comparison of pathways (ii) and (vi). Both involve a cooling rate of ~500 °C Ma⁻¹ which ceases at 0.8 Ma ago for pathway (ii), and at present-day for pathway (vi). While a sample following pathway (ii) experiences 10 °C Ma⁻¹ in the last 0.8 Ma and leads to a field-saturated trap filling, a sample following pathway (vi) experiences ~500 °C Ma⁻¹ in the past 0.2 Ma and is thus dateable. Non-saturated IRSL₅₀ systems may therefore be regarded as good indicators of either prolonged storage at high ambient temperatures (>32 °C), or young and rapid

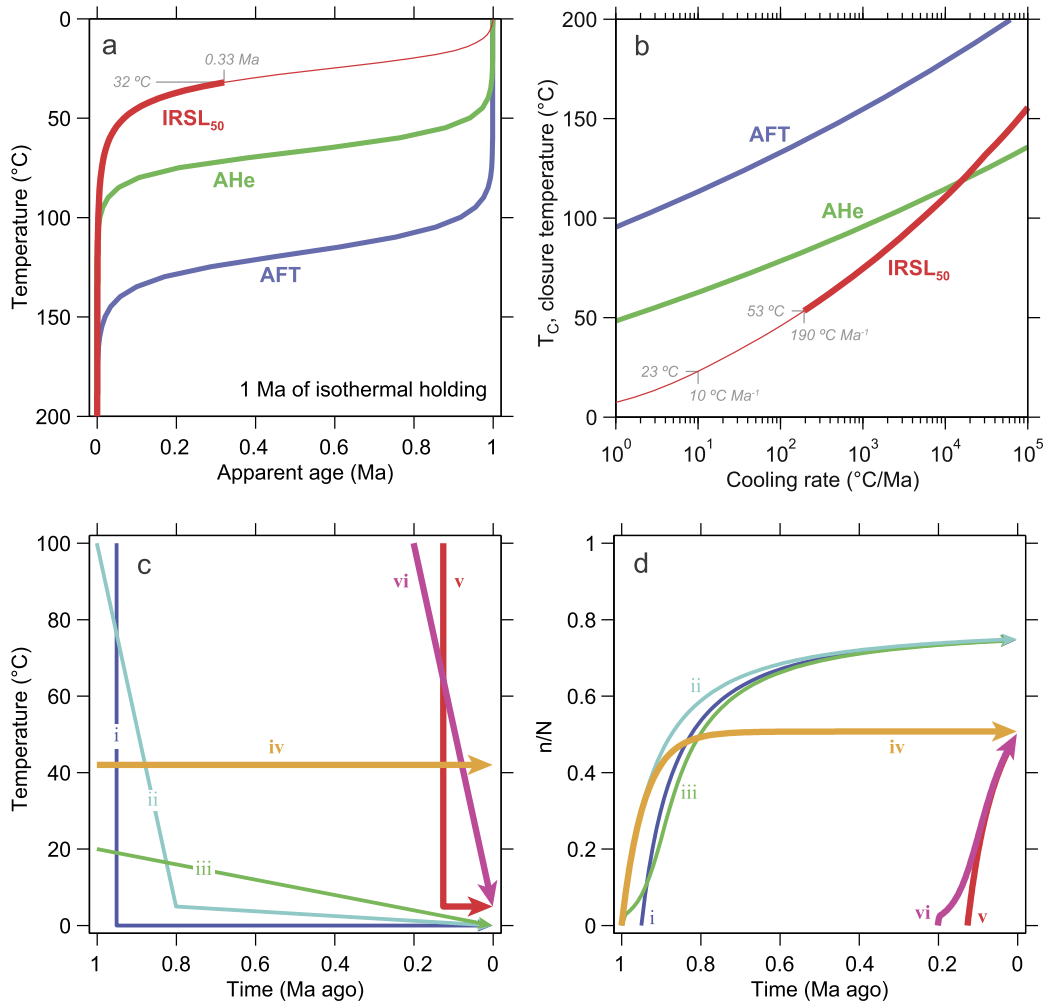


Fig. 5. Upper panels: methodological comparison of Na-feldspar IRSL₅₀ (kinetic parameters from Table 3) with apatite (U-Th)/He (AHe), with Arrhenius parameters $E_a = 138 \text{ kJ mol}^{-1}$ and $\Omega = 7.64 = 10^7 \text{ s}^{-1}$ (after Reiners and Brandon, 2006) and apatite fission track (AFT), with $E_a = 147 \text{ kJ mol}^{-1}$ and $\Omega = 2.05 = 10^6 \text{ s}^{-1}$ (after Reiners and Brandon, 2006). (a) Downhole apparent ages resulting after 1 Ma of isothermal holding (starting from $n_0 = 0$). (b) Closure temperatures T_C for a final temperature of cooling $T_P = 0^\circ\text{C}$ (Guralnik et al., 2013); the thin line segment of the IRSL₅₀ T_C curve corresponds to field-saturated signals beyond dating (Guralnik et al., 2013). Lower panels: arbitrary thermal scenarios (c) and their simulated evolution of trap filling (d), leading to three field-saturated (thin lines marked i–iii) and three dateable (thick lines marked iv–vi) IRSL₅₀ signals.

cooling events ($>190^\circ\text{C Ma}^{-1}$ in the past $<0.33 \text{ Ma}$), or a combination thereof.

6. Discussion

In this work, the natural and non-saturated intensities of Na-feldspar IRSL₅₀ from seven depth samples (1.1–2.3 km depth) have been successfully inverted into a geothermal palaeogradient of $29 \pm 2^\circ\text{C km}^{-1}$, representing a time-averaged estimate over the last $\sim 65 \text{ ka}$, and confirmed by its independent present-day in-situ measurements. This result is methodologically akin to the inference of a $2 \pm 2^\circ\text{C m}^{-1}$ palaeogradient in lunar regolith (Hoyt et al., 1971), or of a $15\text{--}20^\circ\text{C mm}^{-1}$ palaeogradient in meteoritic fusion crusts (Sears, 1975), but is probably the first successful application of the same methodology to infer a known thermal gradient in the shallow crust of Earth. The successful validation of Na-feldspar IRSL₅₀ thermochronometer in a well-constrained thermal setting (KTB) makes us enthusiastic regarding this method as promising for unravelling the thermal structure and history of less thermally-constrained environments, where the estimation of a long-term and artificially-undisturbed thermal structure may be critical, as in the case of correct evaluation of hydrothermal energy resources (e.g. Danis, 2014 and references therein).

The shortfall of Na-feldspar IRSL₅₀ to reconstruct palaeotemperatures in thermal environments colder than $\sim 40^\circ\text{C}$ is due to the fact, that trapped charge systems are governed by two characteristic lifetimes: meaningful palaeotemperature can be recovered only when the lifetime of thermal loss ($s^{-1}e^{E/k_B T}$) in Eq. (1) is, or has recently been, significantly shorter than the lifetime of trap repopulation (D_0/\dot{D}); the violation of this condition inevitably leads to field-saturation (see Eq. (A.9b) in Guralnik et al., 2013) and the consequent loss of any thermal information. For average kinetic parameters and environmental dose rates of Na-feldspar IRSL₅₀ at the KTB (Table 3), the relative importance of these lifetimes tips over at $\sim 30^\circ\text{C}$, suggesting that hydrothermally-active regions or deserts with extreme surface temperatures might open interesting possibilities for feldspar IRSL₅₀ thermochronometry. However, even in ‘cold’ environmental settings, Na-feldspar IRSL₅₀ from underground rocks has the potential to provide critical information on young ($<0.3 \text{ Ma}$) thermal histories of hydrocarbon reservoirs, nuclear waste repositories, and hydrothermal energy fields. Furthermore, non-saturated IRSL₅₀ ages in surface bedrock should be regarded as substantial evidence of either extraordinarily rapid erosion (e.g. Herman et al., 2010), or of recent hydrothermal anomalies (e.g. Takashima, 1979), and can therefore be used in

geothermal prospecting alongside noble-gas and fission track thermochronometers (Reiners and Ehlers, 2005).

Feldspar IRSL₅₀ signals presented in this study are characterised by athermal fading (Huntley, 2006), whose lifetime ($s^{-1}e^{\rho'-1/3\rho'}$) further narrows the thermal sensitivity of feldspar IRSL₅₀ at low temperatures due to purely athermal losses (competing with the thermal depletion pathway). Although weakly- or non-fading IRSL signals (Li and Li, 2011; Buylaert et al., 2012; Jain et al., 2015) present an interesting alternative, the higher-stimulation temperature protocols typically extract signals with higher thermal activation energies (Sohbati et al., 2013; Guralnik et al., 2015b) and thus might eventually be unsuitable for low-temperature thermochronometry. The fact, that Na-feldspar post-IR IRSL₂₉₀ in our top (0.1 km) and bottom (2.3 km) samples were indistinguishable from each other, attests to an unfortunate entanglement: although the post-IR IRSL₂₉₀ signals may not require a fading correction, their thermal sensitivity appears to lie at higher temperatures. While intermediate-stability post-IRSL signals (Li and Li, 2011), thermally-transferred IRSL (Reimann et al., 2015) or pulsed IRSL₅₀ (Jain et al., 2015) may offer a better compromise between thermal and athermal stabilities than those of the veteran IRSL₅₀ protocol used here, such signal optimisation remains to be tested in future works.

7. Conclusions

This study explored the potential of OSL-thermochronometry in a natural and well-constrained thermal setting (the KTB borehole, Germany). The luminescence behaviour of different minerals from twelve metamorphic bedrock samples (0.1–2.3 km depth) suggests that quartz OSL is dim and insensitive, while feldspar IRSL₅₀ signals are bright and comparable to those found in sedimentary environments, promoting their further use. Through extensive mineralogical investigation, the extracted feldspar was characterised as predominantly Na-feldspar, although we accounted also for the possibility that K-feldspar veins and/or inclusions contributed to the IRSL₅₀ signal. Fading-corrected ages in the borehole vary between field saturated ages of >0.3 Ma in the top ~1 km, decreasing to ~14 ka at 2.3 km depth, revealing a partial retention zone of ~40–65 °C.

The inversion of Na-feldspar IRSL₅₀ intensities into apparent environmental temperatures required an in-depth laboratory characterisation of electron trapping and of thermal and athermal (fading) electron detrapping across 3–4 orders of magnitude of time, extending typical luminescence measurements carried out in standard dating applications. The laboratory IRSL₅₀ behaviour could be well described by a combination of a general-order trapping-detrapping formulation with an athermal fading model, whose joint extrapolation to natural conditions (~10 orders of magnitude beyond laboratory observations) recovered sensible palaeotemperatures, further confirmed by independent measurements. However, the presented kinetic model should be seen only as an initial step towards a more elaborate physical formulation incorporating additional dosimetric variables and second-order effects.

Although the applicability of feldspar IRSL₅₀ to resolve exhumation rates appears to be limited only to exceptionally rapid cooling environments (>200 °C Ma⁻¹), the combination of thermal sensitivity at low temperatures >35 °C with rapid equilibration times <0.3 Ma suggests an unprecedented tool for reconstructing the palaeotemperature of shallow subsurface environments, such as utility tunnels, medium enthalpy geothermal resources, young hydrocarbon reservoirs, and nuclear waste repositories. We believe that despite the limitations of the presented feldspar IRSL₅₀ signal, our work will stimulate further exploration of other signals, that may extend the usable range of luminescence thermochronometry.

Acknowledgements

This work is the product of Swiss National Foundation grant 200021-127127 to FH, and constitutes the central chapter of BC's doctoral dissertation at ETH-Zürich. PGV was funded by SNF PZ00P2-148191/1, and CA by NWO-VENI-863.13.023. F. Holzförster and U. Lauterbach helped with sample acquisition, R. Sohbati and J.-P. Buylaert assisted in the laboratory, and Y. Guralnik contributed statistical expertise. We thank M.T. Brandon, D.J. Huntley, D.C.W. Sanderson, and K. Gallagher for insightful feedback on work in progress, and all HAZARD participants for fruitful discussions on feldspar luminescence. D.L. Shuster, R. Grün, anonymous reviewers, and the Editor provided thoughtful comments that greatly improved the manuscript. This paper is dedicated to the dear memory of Lea Honigstein, whose legacy supported the first geological excursion of BG to Germany in 2005.

Appendix A. Supplementary material

Supplementary material related to this article can be found online at <http://dx.doi.org/10.1016/j.epsl.2015.04.032>.

References

- Aitken, M.J., 1998. *An Introduction to Optical Dating: The Dating of Quaternary Sediments by the Use of Photon-Stimulated Luminescence*. Oxford University Press, 267 pp.
- Auclair, M., Lamothe, M., Huot, S., 2003. Measurement of anomalous fading for feldspar IRSL using SAR. *Radiat. Meas.* 37, 487–492.
- Bøtter-Jensen, L., Thomsen, K.J., Jain, M., 2010. Review of optically stimulated luminescence (OSL) instrumental developments for retrospective dosimetry. *Radiat. Meas.* 45, 253–257.
- Buylaert, J.P., Huot, S., Murray, A.S., van den Haute, P., 2011. Infrared stimulated luminescence dating of an Eemian (MIS 5e) site in Denmark using K-feldspar. *Boreas* 40, 46–56.
- Buylaert, J.P., Jain, M., Murray, A.S., Thomsen, K.J., Thiel, C., Sohbati, R., 2012. A robust feldspar luminescence dating method for Middle and Late Pleistocene sediments. *Boreas* 41, 435–451.
- Chen, R., Pagonis, V., 2011. *Thermally and Optically Stimulated Luminescence: A Simulation Approach*. Wiley, UK, 434 pp.
- Christodoulides, C., Ettinger, K.V., Fremlin, J.H., 1971. The use of TL glow peaks at equilibrium in the examination of the thermal and radiation history of materials. *Mod. Geol.* 2, 275–280.
- Clauser, C., Giese, P., Huenges, E., Kohl, T., Lehmann, H., Ryback, L., Safanda, J., Wilhelm, H., Windlof, K., Zoth, G., 1997. The thermal regime of the crystalline continental crust: implications from the KTB. *J. Geophys. Res.* 102, 18417–18441.
- Coyne, D.A., Wagner, G.A., Hejl, E., Brown, R., Van den Haute, P., 1997. The cretaceous and younger thermal history of the KTB site (Germany) apatite fission-track data from the Vorbohrung. *Geol. Rundsch.* 86, 203–209.
- Danis, C., 2014. Use of groundwater temperature data in geothermal exploration: the example of Sydney Basin, Australia. *Hydrogeol. J.* 22, 87–106.
- Dodson, M.H., 1973. Closure temperature in cooling geochronological and petrological systems. *Contrib. Mineral. Petrol.* 40, 259–274.
- Durrani, S.A., Khazal, K.A.R., Ali, A., 1977. Temperature and duration of the shadow of a recently-arrived lunar boulder. *Nature* 266, 411–415.
- Durrani, S.A., Prachyabrued, W., Christodoulides, C., Fremlin, J.H., Edgington, J.A., Chen, R., Blair, I.M., 1972. Thermoluminescence of Apollo 12 samples: implications for lunar temperature and radiation histories. In: *Proc. 3rd Lunar Sci. Conf.*, vol. 3, pp. 2955–2970.
- Durrani, S.A., Prachyabrued, W., Hwang, F.S.W., Edgington, J.A., Blair, I.M., 1973. Thermoluminescence of some Apollo 14 and 16 fines and rock samples. In: *Proc. 4th Lunar Sci. Conf.*, vol. 4, pp. 2465–2479.
- Grögler, N., Houtermans, F.G., Stauffer, H., 1958. The use of thermoluminescence for dosimetry and research on the radiation and thermal history of solids. In: *Proc. 2nd Int. Conf. on the Peaceful Uses of Atomic Energy*. Geneva, vol. 21. United Nations, New York, pp. 226–229.
- Grün, R., 2001. Trapped charge dating (ESR, TL, OSL). In: Brothwell, D.R., Pollard, A.M. (Eds.), *Handbook of Archaeological Sciences*. John Wiley & Sons Inc., West Sussex, England, pp. 47–62.
- Grün, R., Tani, A., Gurbanov, A., Koshchug, D., Williams, I., Braun, J., 1999. A new method for the estimation of cooling and rates using paramagnetic centers in quartz: a case study on the Eldzhurtinskiy Granite, Caucasus. *J. Geophys. Res.* 104, 17531–17549.

- Guérin, G., Mercier, N., Nathan, R., Adamiec, G., Lefrais, Y., 2012. On the use of the infinite matrix assumption and associated concepts: a critical review. *Radiat. Meas.* 47, 778–785.
- Guralnik, B., Ankjærgaard, C., Jain, M., Murray, A.S., Müller, A., Wälle, M., Lowick, S.E., Preusser, F., Rhodes, E.J., Wu, T.-S., Mathew, G., Herman, F., 2015a. OSL-thermochronometry using bedrock quartz: a note of caution. *Quat. Geochronol.* 25, 37–48.
- Guralnik, B., Jain, M., Herman, F., Paris, R.B., Harrison, T.M., Murray, A.S., Valla, P.V., Rhodes, E.J., 2013. Effective closure temperature in leaky and/or saturating thermochronometers. *Earth Planet. Sci. Lett.* 384, 209–218.
- Guralnik, B., Li, B., Jain, M., Chen, R., Paris, R.B., Murray, A.S., Li, S.-H., Pagonis, V., Valla, P.G., Herman, F., 2015b. Radiation-induced growth and isothermal decay of feldspar IRSL. *Radiat. Meas.* <http://dx.doi.org/10.1016/j.radmeas.2015.02.011>.
- Herman, F., Rhodes, E.J., Braun, J., Heiniger, L., 2010. Uniform erosion rates and relief amplitude during glacial cycles in the Southern Alps of New Zealand, as revealed from OSL-thermochronology. *Earth Planet. Sci. Lett.* 297, 183–189.
- Hirschmann, G., Duyster, J., Harms, U., Kontny, A., Lapp, M., De Wall, H., Zulauf, G., 1997. The KTB superdeep borehole: petrography and structure of a 9-km-deep crustal section. *Geol. Rundsch.* 86, S3–S14.
- Houtermans, F.G., Jäger, E., Schön, M., Stauffer, H., 1957. Messungen der Thermolumineszenz als Mittel zur Untersuchung der thermischen und der Strahlungsgeschichte von natürlichen Mineralien und Gesteinen. *Ann. Phys.* 20, 283–292.
- Hoyt Jr., H.P., Miyajima, M., Walker, R.M., Zimmerman, D.W., Zimmerman, J., Britton, D., Kardos, J.L., 1971. Radiation dose rates and thermal gradients in the lunar regolith: thermoluminescence and DTA of Apollo 12 samples. In: *Proc. 2nd Lunar Sci. Conf.*, vol. 3, pp. 2245–2263.
- Huntley, D.J., 2006. An explanation of the power-law decay of luminescence. *J. Phys. Condens. Matter* 18, 1359–1365.
- Huntley, D.J., Lian, O.B., 2006. Some observations on tunnelling of trapped electrons in feldspars and their implications for optical dating. *Quat. Sci. Rev.* 25, 2503–2512.
- Hütt, G., Jaek, I., Tchonka, J., 1988. Optical dating: K-feldspars optical response stimulation spectra. *Quat. Sci. Rev.* 7, 381–385.
- Ikeya, M., Miki, T., Tanaka, K., 1982. Dating of a fault by electron spin resonance on intrafault materials. *Science* 215, 1392–1393.
- Iman, R.L., Conover, W.J., 1982. A distribution-free approach to inducing rank correlation among input variables. *Comm. Stat. B-Simul.* 11, 311–334.
- Jain, M., Buylaert, J.P., Thomsen, K.J., Murray, A.S., 2015. Further investigations on 'non-fading' in K-Feldspar. *Quat. Int.* 362, 3–7.
- Johnson, N.M., 1963. Thermoluminescence in contact metamorphosed limestone. *J. Geol.* 71, 596–616.
- Kars, R.H., Wallinga, J., Cohen, K.M., 2008. A new approach towards anomalous fading correction for feldspar IRSL dating – tests on samples in field saturation. *Radiat. Meas.* 43, 786–790.
- Li, B., Li, S.-H., 2011. Luminescence dating of K-feldspar from sediments: a protocol without anomalous fading correction. *Quat. Geochronol.* 6, 468–479.
- Lovering, T.G., 1958. Temperatures and depth of formation of sulfide ore deposits at Gilman, Colorado. *Econ. Geol.* 53, 689–707.
- Murray, A.S., Buylaert, J.P., Thomsen, K.J., Jain, M., 2009. The effect of preheating on the IRSL signal from feldspar. *Radiat. Meas.* 44, 554–559.
- Prokein, J., Wagner, G.A., 1994. Analysis of thermoluminescent glow peaks in quartz derived from the KTB-drill hole. *Radiat. Meas.* 23, 85–94.
- Reimann, T., Ankjærgaard, C., Wallinga, J., 2015. Testing the potential of a transferred IRSL (T-IRSL) feldspar signal for luminescence dating. *Radiat. Meas.* <http://dx.doi.org/10.1016/j.radmeas.2015.01.002>.
- Reiners, P.W., Brandon, M.T., 2006. Using thermochronology to understand orogenic erosion. *Annu. Rev. Earth Planet. Sci.* 34, 419–466.
- Reiners, P.W., Ehlers, T.A., 2005. Low-temperature thermochronology: techniques, interpretations, applications. *Rev. Mineral. Geochem.* 58, 622.
- Ronca, L.B., Zeller, E.J., 1965. Thermoluminescence as a function of climate and temperature. *Am. J. Sci.* 263, 416–428.
- Sears, D.W., 1975. Temperature gradients in meteorites produced by heating during atmospheric passage. *Mod. Geol.* 5, 155–164.
- Sohbati, R., Murray, A., Jain, M., Thomsen, K., Hong, S.C., Yi, K., Choi, J.H., 2013. Na-rich feldspar as a luminescence dosimeter in infrared stimulated luminescence (IRSL) dating. *Radiat. Meas.* 51–52, 67–82.
- Takashima, I., 1979. Preliminary study on the determination of alteration age by a thermoluminescence method. *Bull. Geol. Surv. Japan* 30, 285–295.
- Wallinga, J., Murray, A.S., Wintle, A., 2000. The single-aliquot regenerative-dose (SAR) protocol applied to coarse-grain feldspar. *Radiat. Meas.* 32, 529–533.
- Wallinga, J., Murray, A.S., Wintle, A.G., Bøtter-Jensen, L., 2002. Electron-trapping probability in natural dosimeters as a function of irradiation temperature. *Radiat. Prot. Dosim.* 101, 339–344.
- Warnock, A.C., Zeitler, P.K., 1998. $^{40}\text{Ar}/^{39}\text{Ar}$ thermochronometry of K-feldspar from the KTB borehole, Germany. *Earth Planet. Sci. Lett.* 158, 67–79.
- Warnock, A.C., Zeitler, P.K., Wolf, R.A., Bergman, S.C., 1997. An evaluation of low temperature apatite U–Th/He thermochronometry. *Geochim. Cosmochim. Acta* 61, 5371–5377.
- Wolfe, M.R., Stockli, D.F., 2010. Zircon (U–Th)/He thermochronometry in the KTB drill hole, Germany, and its implications for bulk He diffusion kinetics in zircon. *Earth Planet. Sci. Lett.* 295, 69–82.
- Ypma, P.J., Hochman, M., 1991. Thermoluminescence geothermometry – a case study of the Otway Basin. *APEA J.* 35, 312–324.